# Enhanced Hong-Ou-Mandel manifolds and figures of merit for linear chains of identical microring resonators

Peter L. Kaulfuss [1,2,*] Paul M. Alsing [1] A. Matthew Smith [1] Joseph Monteleone, III,[2] and Edwin E. Hach, III [2]

[1]*Information Directorate, Air Force Research Laboratory, 525 Brooks Road, Rome, New York 13411, USA*

[2]*School of Physics and Astronomy, Rochester Institute of Technology, 85 Lomb Memorial Drive, Rochester, New York 14623, USA*

We present an exact analytic expression for the Hong-Ou-Mandel manifold (HOMM) for any number of identical microring resonators (MRRs) in a linear chain. The HOMM is the higher-dimensional manifold of solutions for which the HOM effect is obtained; for the types of MRR systems investigated in this work, it is a one-dimensional curve. We investigate the extreme stability of this HOMM, showing that the HOM effect in linear arrays of MRRs is highly robust. We further use this expression to derive three figures of merit for the HOMM of linear chains of MRRs: the minimum MRR coupling value $\tau_c$, the curvature of the one-dimensional HOMM $\bar{\xi}_N$, and the 5% tolerance in the probability for complete destructive interference to occur on the HOMM $\delta\tau_N$. We promote these metrics to characterize the pros and cons of various linear chains of MRRs and inform design and fabrication.

## I. INTRODUCTION

The Hong-Ou-Mandel (HOM) effect, originally discovered in 1987 as the essential phenomenon underlying then ground-breaking subpicosecond time delay measurements [1–5], remains a central tool for a wide and growing variety of quantum applications.

The enduring interest in the HOM effect proceeds from its role as a deterministic method for generating and manipulating two-photon entanglement, a valuable resource for quantum information processing [6–9], especially quantum computing [10]. Owing to the measurement-induced nonlinearity resulting from postselective techniques applied to the HOM output, it plays a crucial role in the operation of probabilistic universal gates such as the controlled-*Z* (CZ) [10,11] and the controlled-NOT (CNOT) [12–14] gates.

The HOM effect is important to the implementation of many specific applications in quantum computation relying upon single-algorithm devices. Fisher *et al.* showed computation on encrypted data [15], and Harrow *et al.* and Cai *et al.* used quantum algorithms to solve systems of linear equations [16,17]; the computation of discrete and fractional Fourier transforms was shown by Weimann *et al.* [18], and Humphreys *et al.* showed linear optical quantum computing on a single spatial mode [19].

The HOM interference visibility is useful for evaluating the level of indistinguishability of photons from a variety of single-photon sources. Kaltenbaek *et al.* and Mosley *et al.* used this technique for spontaneous parametric down-conversion sources [20,21]. Numerous groups have used this method to investigate photons produced by quantum dots [22–26], atomic vapors [27–31], nitrogen-vacancy centers in diamond [32–34], molecules [35,36], trapped neutral atoms [37,38], and trapped ions [39]. The HOM effect is widely applied in quantum communication and quantum cryptography [40,41]. Commercial quantum key distribution (QKD) systems have been shown experimentally to be vulnerable to several side channel attacks [42,43]. One proposed solution to overcome these security issues is a full-device-independent QKD scheme [44,45], but its requirements are difficult to meet, and it yields low secret key rates, which is why the measurement-device-independent protocol was developed [46,47]. The measurement-device-independent QKD protocol involves making a Bell state measurement by making photons arrive simultaneously on a beam splitter and observing the interference to establish the keys [11,46,47]. Liu *et al.* demonstrated this measurement-device-independent protocol experimentally using time-bin phase-encoding [48]. For example, the passive round-robin differential phase-shift QKD protocol discussed by Guan *et al.* also capitalizes on the HOM effect [49]. Common schemes in quantum communication and quantum cryptography, such as quantum teleportation and entanglement swapping, rely on the HOM-induced entanglement [50,51]. Quantum repeaters can be used in tandem with Bell state analyzers to entangle pairs of atoms which can then be used for these QKD protocols [52]. QKD appears to allow the exchange of secret information that cannot be intercepted, but security loopholes have been found in practical implementations [53,54].

Fabrication defects in large integrated devices containing multiple sequential devices such as Mach-Zehnder meshes remain an outstanding problem [55–57]. We compare our devices to a directional coupler tolerance of 5% [58]. This is based on a 193 nm UV lithography standard [59], although

many fab shops use older processes. This can result in a splitting ratio varying by several percent. Our devices show better tolerances to fabrication errors.

Here, we are motivated by the global perspective that theoretical proposals for enhancing the parametric flexibility of photonic HOM elements will directly impact many, if not all, applications relying on the HOM effect in such an architecture. One example of this sort of enhancement was presented earlier by the present authors in the form of higher-dimensional Hong-Ou-Mandel manifolds (HOMMs) within the parameter space of a double-bus microring resonator (DB-MRR) [60].

The MRR can be thought of as taking a beam splitter (one parameter) and expanding it into (in general) three parameters ("top" and "bottom" directional couplers and an internal phase angle), which are coupled together to form higher-dimensional manifolds in which the HOM destructive interference condition can be met (vs the single-point solution associated with a beam splitter [60,61]; see Appendix C for a more complete discussion of this point). We use the term "Hong-Ou-Mandel manifold" to describe these higher-dimensional solution sets in parameter space. The extension to linear chains of MRRs allows for further design optimization to consider coupling and phase stability. MRRs also provide increased scalability and tunability over a simple beam splitter.

We examine significant enhancements to the HOMM that arise as a result of fabricating a relatively simple photonic circuit comprising a serial chain of identical, balanced MRRs, and we propose, in connection with them, three figures of merit informing the design, fabrication, and characterization of any such structure in the context of a wide variety of applications.

The outline of the paper is as follows: in Sec. II we define our approach to characterizing the HOM effect in an MRR, present the exact analytic solution of the one-dimensional HOMM for any number of MRRs in series, and define our first figure of merit, $\tau_c$, the minimum MRR coupling value to achieve the HOM effect. In Sec. III we investigate the phase stability of our one-dimensional HOMM and define our second figure of merit, $\bar{\xi}_N$, the curvature of the one-dimensional HOMM. In Sec. IV, we then investigate the coupling stability of our one-dimensional HOMM and define our last figure of merit, $\delta\tau_N$, the 5% tolerance in the probability for complete destructive interference to occur on the HOMM. Finally, in Sec. V we summarize our results and describe how these three figures of merit can be used in combination to inform design and fabrication. We also include, in Appendix A, a review of the evanescent couplers used in this DB-MRR and, in Appendix B, a more detailed derivation of our main result, the exact analytic expression of the one-dimensional HOMM for any number of MRRs in series.

## II. MRR HOMM RESULTS

Figure 1 shows a schematic representation of such a chain, indicating the notation that we adopt. We define the chain length of the circuit as $N$, the number of identical MRRs in the chain. The MRRs are identical, each having a common round-trip phase shift $\theta_j \to \theta$ and equal transmission and
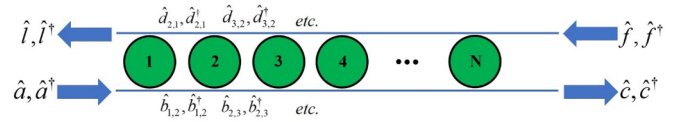


FIG. 1. A serial chain of identically coupled, identical double-bus MRRs; the input modes are $a$ and $f$, and the output modes are $c$ and $l$. The internal modes, $b$ and $d$, enter into the derivation of the HOM Manifolds, but they do not enter explicitly into the results.

reflection coefficients $(\tau_j, \kappa_j, \gamma_j, \eta_j) \to (\tau, \kappa, \gamma, \eta)$, and are balanced, i.e., $\kappa = \gamma$ and $\tau = \eta$. We invoke here the labeling scheme introduced in [60] for the coupling parameters; these are reviewed in Appendix A. Further, we adopt the phase convention in which

$$\tau = \tau^* = |\tau|, \quad \kappa = i\sqrt{1 - |\tau|^2} = i\sqrt{1 - \tau^2}. \quad (1)$$

The phases indicated in Eq. (1) ensure the satisfaction of the reciprocity relations for each directional coupler [62], and they allow us to characterize the linear chain using the three real parameters $(\tau, \theta, N$; see Appendix A). The one-dimensional HOMM of a chain of length $N$ is then given by the curve $\tau_N(\theta)$ (see Appendix B). Our prior work in [60] then serves as the $N = 1$ basis for comparison and characterization of our results for arbitrary chain lengths.

Owing to the linearity of the medium (negligible absorption), the evanescent nature of the coupling (negligible scattering), and the low intensities of the photons (negligible photonic losses), we work here in the lossless regime. As we show below, for many applications chain lengths of 2–3 are optimal, justifying the lossless approximation for short chains. We previously presented analyses of losses in the "unit cell" DB-MRR [61,63,64]. The lesson from that work was that parametric HOMM structures (see Fig. 3 below) are persistent within reasonable experimental tolerances even in the presence of realistic loss mechanisms.

One way to formulate the one-dimensional HOMM for a serial chain of length $N > 1$ is to use the result that we have derived based upon a discrete path integral (DPI) for the $N = 1$ case [60,65], along with the relevant application of the "mode-swap algebra" that we described previously in proposing a scalable CNOT gate [13]. Figure 1 explicitly displays the operators, represented as quantum interconnects along each of the waveguides between the MRRs. These operators, $\{\hat{d}_{j,i}, \hat{b}_{i,j}\}$, must then be algebraically eliminated in order to produce the desired "$S$ matrix" relating the input and outputs for the chain as a whole.

Using this approach along with mathematical induction [13,60], one can show (see Appendix B) analytically that the probability for output photon coincidence from the system represented in Fig. 1 is given by

$$P_{1,1}(\tau, \theta; N) = \frac{(1 - 4\tau^{2N} + \tau^{4N} + 2\tau^{2N}\cos\theta)^2}{(1 + \tau^{4N} - 2\tau^{2N}\cos\theta)^2}. \quad (2)$$

The HOM constraint can be expressed using

$$P_{1,1}(\tau, \theta; N) = 0. \quad (3)$$

For a chain of length $N$, Eq. (3) defines a one-dimensional HOMM, $\tau_N(\theta)$. After some more algebra, we find that the
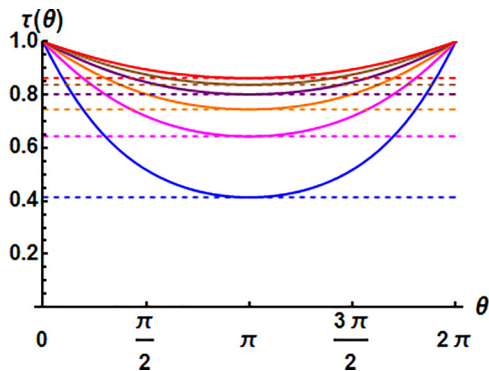
FIG. 2. : One-dimensional HOM manifolds for chains of identical MRRs with lengths $N = 1$ (blue), 2 (magenta), 3 (orange), 4 (purple), 5 (brown), and 6 (red). The horizontal lines indicate the HOM cutoff value for the coupling parameter for each chain.

physical one-dimensional HOMM for the serial chain of length $N$ is given in closed form by

$$\tau_N(\theta) = (2 - \cos\theta - \sqrt{3 - 4\cos\theta + \cos^2\theta})^{\frac{1}{2N}}. \quad (4)$$

Equation (4) encodes the principal result of this work. We now use this result to motivate our proposals for three figures of merit characterizing the practical implementation of the HOM effect in integrated nanophotonics.

In Fig. 2 we plot the one-dimensional (1D) HOMM for several chain lengths, including, for comparison, the $N = 1$ case [60]. Several important features are apparent. First, the 1D HOMMs are all symmetric in $\tau$ about a round-trip phase shift of $\theta_0 = \pi$. This phase shift turns out to be especially important in what follows, so we have labeled it with a subscript.

Second, the cutoff coupling parameter below which the HOM effect never occurs in the device increases monotonically with chain length. It is straightforward to determine this trend analytically,

$$\tau_c = (3 - \sqrt{8})^{\frac{1}{2N}}, \quad (5)$$

as shown by the horizontal lines in Fig. 2. The HOM effect is clearly attainable over the experimentally feasible range of couplings $0.5 \leqslant \tau \leqslant 0.9$, easily bracketing the important case of the 3 dB coupler, $\tau_{3dB} = \frac{1}{\sqrt{2}}$.

## III. HOM PHASE STABILITY

It is apparent from Fig. 2 that the 1D HOMM is particularly flat for any chain length near the point $(\tau_c, \theta_0 = \pi)$, which we shall refer to as the optimal operating point for implementation of the HOM effect. This flatness suggests a high degree of parametric stability in the HOM effect from a linear chain operating near this point compared to a directional coupler [59]. The stability of this nature in concert with the inherent tunability of the silicon nanophotonic architecture implies a potentially large advantage for deploying HOM-based elements on scalable platforms.

To make this more precise, we expand the coincidence probability given by Eq. (2) in $\tau$ and $\theta$ to the lowest nonvan-

ishing order about the optimal operating point,

$$P_{1,1}(\tau, \theta; N) \approx \frac{1}{2} \frac{\partial^2 P_{1,1}}{\partial \tau^2}\bigg|_0 (\tau - \tau_c)^2 + \frac{1}{24} \frac{\partial^4 P_{1,1}}{\partial \theta^4}\bigg|_0 (\theta - \pi)^4. \quad (6)$$

An evaluation of the nonvanishing expansion coefficients appearing in Eq. (6) is straightforward but not enlightening. Instead, the important features that emerge are that the HOM effect near the optimal operating point is stable to second order in the coupling parameter and to fourth order in the round-trip phase shift. The HOM stability in $\theta$ is especially striking; it is evident that linear chains of identical DB-MRRs share a universal third-order HOM stability when operated near the cutoff coupling, making the structure especially robust there against parametric drift due to environmental conditions. Motivated by this, we identify the cutoff value of the directional coupling parameter $\tau_c$ itself as one figure of merit characterizing the HOM performance of this class of integrated photonic structure.

Once again referring to Fig. 2, we can extend the notion of local HOM parametric stability near the optimal operating point to the global concept of HOM device stability. The round-trip phase shift for a photon with angular frequency $\omega$ propagating through an MRR with radius $R$ is given by

$$\theta = 2\pi \frac{n(\omega)R}{c}\omega, \quad (7)$$

where $n(\omega)$ is the linear index of the refraction of silicon. If we imagine the operating conditions for a chain of length $N$ wherein the HOM effect occurs with unit fidelity for a given photon angular frequency $\omega$ and assuming that the coupling is independent of small changes in the frequency $\delta\omega$, we see that the flatter the HOMM $\tau_N(\theta(\omega))$ is, the larger the residual HOM fidelity over the support of the frequency spectrum for input photons is. A shift $\delta\omega$ in photon frequency induces a round-trip phase shift of

$$\delta\theta = 2\pi \frac{n(\omega)R}{c}\delta\omega, \quad (8)$$

where we have assumed a flat dispersion relation for silicon over the relevant range of angular frequencies. Expanding the photon coincidence probability in MRR round-trip phase shift to the lowest nonvanishing order about any given point on the 1D HOMM for the chain gives

$$P_{1,1}(\tau_N(\theta), \theta + \delta\theta; N) \approx \frac{1}{4}\cot^2\left(\frac{\theta}{2}\right)(\delta\theta)^2, \quad (9)$$

where we have explicitly indicated that the value of the coupling parameter is the one appropriate to the point on the HOMM about which we are expanding in $\theta$. Note that Eq. (9) is consistent with Eq. (6) for $\theta \to \pi$; the second-order correction in $\theta$ vanishes there. Equation (9) shows that the HOM stability with respect to the MRR round-trip phase shift is maintained to first order along the entire 1D HOMM. Further, the fact that the second-order correction term given in Eq. (9) is independent of the chain length implies that the local round-trip phase HOM stability at each point on the 1D HOMM is universal to this class of device. In view of Eq. (8), this results in a very high fidelity HOM output from any given serial chain over a nonvanishing range of input photon frequencies. The general design lesson in this is that serial chains with

TABLE I. Characteristics of series of up to 10 identical rings. Here, $\delta\tau_N$ uses a value of $\epsilon_N = 0.05$.

| $N$ | $\tau_c$ | $\bar{\xi}_N$ | $\delta\tau_N$ |
|---|---|---|---|
| 1 | 0.4142 | 0.1424 | 0.1323 |
| 2 | 0.6436 | 0.0772 | 0.1029 |
| 3 | 0.7454 | 0.0523 | 0.0796 |
| 4 | 0.8022 | 0.0395 | 0.0642 |
| 5 | 0.8384 | 0.0317 | 0.0537 |
| 6 | 0.8634 | 0.0264 | 0.0461 |
| 7 | 0.8817 | 0.0227 | 0.0404 |
| 8 | 0.8957 | 0.0199 | 0.0359 |
| 9 | 0.9067 | 0.0177 | 0.0323 |
| 10 | 0.9156 | 0.0159 | 0.0294 |

flatter 1D HOMMs are better suited to accommodate practical achievement of the HOM effect for input photons with finite bandwidths. It is in this sense that the DB-MRR structure, even for $N = 1$, acts as a sort of filter for the HOM effect itself. Whereas HOM fidelity disappears at a beam splitter rapidly when the input photons become nonmonochromatic, the deterioration is much less violent in the MRR-based structure. This is a distinct advantage of this architecture that relies directly on the existence of the HOMM.

Motivated by the universal (at least) first-order HOM stability near the 1D HOMM and the independence from chain length of the lowest-order correction term, we propose a global figure of merit to characterize the "overall flatness" of the HOMM for a chain of length $N$. We characterize the HOM round-trip phase stability of such a device using the average curvature of the 1D HOMM [66]:

$$\bar{\xi}_N \equiv \frac{1}{2\pi} \int_0^{2\pi} \frac{\left| \frac{d^2\tau_N(\theta)}{d\theta^2} \right|}{\left( 1 + \frac{d\tau_N(\theta)}{d\theta} \right)^{\frac{3}{2}}} \, d\theta. \tag{10}$$

Smaller values of $\bar{\xi}_N$ characterize serial chain HOM structures with higher phase stability. Using Eq. (4), one can, in principle, develop a complicated analytical form for $\bar{\xi}_N$; instead, we take the pragmatic approach of numerically computing the average curvature for the 1D HOMM in linear chains with lengths of $N = 1, \ldots, 10$. These results are displayed in Table I. The monotonic trend toward overall flatness is apparent, suggesting that longer chains offer increasing HOM phase stability, which, in view of Eq. (8), suggests persistence in the HOM visibility over broader spectral ranges of input photons.

## IV. HOM COUPLING STABILITY

We now investigate HOM stability against small changes in the coupling parameter $\tau$ about operating points on the 1D HOMM, especially near the optimal operating point, $(\tau_c, \theta_0 = \pi)$. It is easy to show that the lowest-order correction term is of second order in $\tau$ for operation of the linear chain near *any* point on the 1D HOMM,

$$P_{1,1}(\tau, \theta; N) \approx \frac{1}{2} \left. \frac{\partial^2 P_{1,1}}{\partial \tau^2} \right|_{\text{HOMM}} [\tau - \tau_N(\theta)]^2. \tag{11}$$

Near the optimal operating point, this result assumes the form

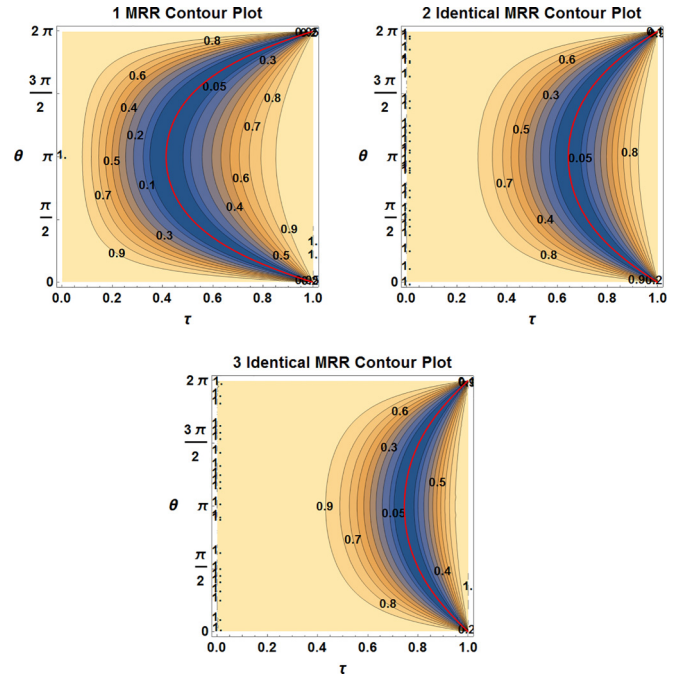$$P_{1,1}(\tau, \theta_0; N) \approx \frac{2N^2(\tau - \tau_c)^2}{\tau_c^2}. \tag{12}$$



FIG. 3. Contour plots of $P_{1,1}(\tau, \theta; N)$ vs $\tau$ and $\theta$ for chains with lengths $N = 1$ (top left), $N = 2$ (top right), and $N = 3$ (bottom). The red curve in each contour plot is the exact curve of zero probability, described by Eq. (4). These crescent-shaped plots are qualitatively similar for chains of all lengths.

One can use Eqs. (2) and (4) to arrive at a closed form for the general, second-order expansion coefficient in $\tau$, as indicated in Eq. (11), but this form is cumbersome, so we omit it here.

In order to characterize the HOM coupling stability for a linear chain, we consider in Fig. 3 contour plots of the output photon coincidence probability versus the coupling parameter and the round-trip phase shift for chains having lengths of 1, 2, and 3. The basic "crescent" shape prevalent in Fig. 3 is characteristic of chains of all lengths. The nadir of the valley running though the deepest crescent, shown as a solid red curve on each contour plot, is the 1D HOMM described in Eq. (4). The HOM effect occurs at every point along this red curve.

We pay particular attention to the relatively wide crescent-shaped region between the $P_{1,1} = 0.05$ level curves in each part of Fig. 3. These are the parametric regions in which the HOM effect is obtained with a fidelity of 95% or greater, a level typical of careful experimental measurements [61]. The remarkable HOM stability of the chain is evident in the extent of this high-fidelity region, especially near the optimal operating point. We use this observation as the basis for a figure of merit characterizing the HOM stability in the coupling parameter.

We define the practical HOM-tolerance level for a linear chain of length $N$ to be the probability of an undesired output photon coincidence,

$$\epsilon_N \equiv P_{1,1}, \tag{13}$$

where it is understood that Eq. (13) has meaning only in the neighborhood of an exact HOMM, where $P_{1,1} \ll 1$.

For a given tolerance $\epsilon_N$, the level curves delineating the upper $(+)$ and lower $(-)$ bounds of the HOM region can be computed in exact form to be

$$\tau_N^{(\pm)}(\theta) = \frac{1}{(1 \mp \sqrt{\epsilon_N})^{\frac{1}{2N}}} \{2 - (1 \pm \sqrt{\epsilon_N})\cos\theta - \sqrt{4 - (1 \mp \sqrt{\epsilon_N})^2 - 4(1 \pm \sqrt{\epsilon_N})\cos\theta + (1 \pm \sqrt{\epsilon_N})^2 \cos^2\theta}\}^{\frac{1}{2N}}, \quad (14)$$

which, at its widest near $\theta_0 = \pi$, becomes

$$\tau_N^{(\pm)}(\pi) = \left[ \frac{3 - 2\sqrt{2}\sqrt{(1 \pm \sqrt{\epsilon_N})} \pm \sqrt{\epsilon_N}}{1 \mp \sqrt{\epsilon_N}} \right]^{\frac{1}{2N}}. \quad (15)$$

In order to characterize the general HOM coupling stability within experimental tolerance $\epsilon_N$ for a linear chain of length $N$, we propose a figure of merit defined by

$$\delta\tau_N(\epsilon_N) \equiv |\tau_N^{(+)}(\pi) - \tau_N^{(-)}(\pi)|. \quad (16)$$

We choose this metric motivated by the reasonable assumption that linear chains deployed as HOM-based elements within photonic circuits will be integrated to work near the optimal operating point, where, as we have shown above, a high degree of HOM stability against small design, environmental, and spectral fluctuations can be realized.

## V. CONCLUSION

We summarize the results for several chain lengths in Table I. Our approach in this work has been to introduce useful design parameters for the rather idealized case of identical MRRs, allowing closed-form results, but with the idea that the same set of metrics, computed numerically, will be useful for designing and characterizing the HOM responses from complex MRR-based structures useful for a wide range of scientific and engineering applications.

With Table I in view, we now summarize the utility and importance of the results we have presented in this work. It is clear that, as we progress to longer chains of identical DB-MRRs, there is a three-way competition between the spectral stability (via $\bar{\xi}_N$), the coupling stability (via $\delta\tau_N$), and the minimum coupling $\tau_c$ for which the HOM can be realized. As one considers longer chains, the spectral stability increases ($\bar{\xi}_N$ decreases), the coupling stability for any given NOON state fidelity decreases ($\delta\tau_N$ decreases), and the coupling cutoff creeps toward larger values of transmission for each MRR in the chain.

The HOM effect cannot be obtained at any $\tau$ value less than $\tau_c$ for a given number of MRRs. There is nothing inherently desirable or undesirable about any particular value of $\tau_c$ (since any value is achievable, in theory, due to the extreme tunability of the device), but one must keep in mind that, for example, if using a linear array with five MRRs in it the minimum $\tau$ value, $\tau_c$, that can achieve the HOM effect is $\tau_c \approx 0.84$, as shown in Table I. If such a high $\tau_c$ is unrealistic to maintain for a specific implementation in a device, a linear chain of fewer MRRs should be considered. That is the "merit" in knowing the $\tau_c$ value for each chain length $N$. As long as higher $\tau$ coupling values can be achieved, the design choice is between coupling stability and spectral stability. Each successive MRR added to the linear chain decreases the coupling stability and increases the spectral stability of the HOMM where the HOM effect is achieved.

In view of the many applications for the HOM effect that we have reviewed above, it is easy to imagine various optimizations of this competition for maximizing the efficiency of any HOM implementation within a quantum photonic circuit. For example, for a chain that is to be used near the 3 dB (50/50) coupling point, one is limited to having, at most, two MRRs in the chain. Within that restrictive engineering constraint, however, there is still some design freedom. For a system in which the coupling parameter is very stable and well controlled, it should be preferable to use two series of MRRs for the increase in phase (i.e., spectral) stability they offer in comparison with a similarly coupled individual MRR.

In this work, we have presented three figures of merit that characterize important design and optimization opportunities for a class of scalable structures that can readily be integrated into quantum photonic circuits using fabrication techniques that are already implemented routinely. Given the long and persistent history of the HOM effect as an essential tool for quantum photonics, the work we have presented here has the potential to inform the design, optimization, and implementation of an extremely wide range of photonic networks central to next-generation quantum information processing, sensing, and metrology.

## ACKNOWLEDGMENTS

## APPENDIX A: REVIEW OF THE DB-MRR: EVANESCENT COUPLING PARAMETERS

To provide explicit context for the parameters we use throughout the work, we show in Fig. 4 schematic diagrams for the coupling of a unit cell of the serial chain [Fig. 4(a)] and one of the directional couplers within the unit cell in the general case [Fig. 4(b)].

The directional coupler in Fig. 4(b) is described by the linear mode operator transformation

$$\begin{pmatrix} \hat{b}_{j,j+1} \\ \hat{r} \end{pmatrix} = \begin{pmatrix} \tau_j & \kappa_j \\ -\kappa_j^* & \tau_j^* \end{pmatrix} \begin{pmatrix} \hat{b}_{j-1,j} \\ \hat{l} \end{pmatrix}, \quad (A1)$$

where, using the phase convention we have adopted for the coupling parameters, the bosonic commutation relations are
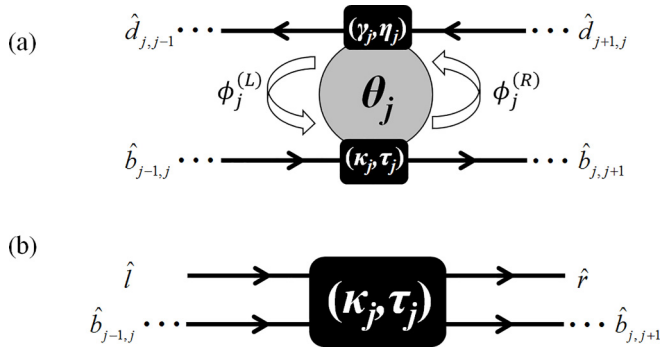
(a)



(b)

FIG. 4. (a) Schematic diagram of the $j$th unit cell for a serial chain of DB-MRRs. This version explicitly displays the general couplings to the waveguides and allows us to reintroduce the parameters we use throughout the body of the work. The directional input-output nature of the device is indicated by the arrows. (b) A close-up view of one of the evanescent couplers; the internal MRR mode operators, $\hat{l}$ and $\hat{r}$, are included to emphasize the input-output ports of the coupler.

enforced by the usual reciprocity relation

$$|\kappa_j|^2 + |\tau_j|^2 = 1, \tag{A2}$$

with analogous relationships describing the coupling at the top of the MRR shown in Fig. 4. Using either the DPI approach we developed in earlier works [60,65] or the boundary value approach [61,67], it is straightforward to show that the operator input-output relations appropriate for the Heisenberg picture description of photon transport through the DB-MRR shown in Fig. 4 are given by the linear system

$$\begin{pmatrix} \hat{b}_{j,j+1}^\dagger \\ \hat{d}_{j,j-1}^\dagger \end{pmatrix} = \begin{pmatrix} T_{11}^{(j)} & T_{12}^{(j)} \\ T_{21}^{(j)} & T_{22}^{(j)} \end{pmatrix} \begin{pmatrix} \hat{b}_{j-1,j}^\dagger \\ \hat{d}_{j+1,j}^\dagger \end{pmatrix}, \tag{A3}$$

where

$$T_{11}^{(j)} = \frac{\eta_j^* - \tau_j e^{i\theta_j}}{\eta_j^* \tau_j^* - e^{i\theta_j}}, \quad T_{12}^{(j)} = \frac{\gamma_j \kappa_j^* e^{i\phi_j^{(L)}}}{\eta_j^* \tau_j^* - e^{i\theta_j}},$$

$$T_{21}^{(j)} = \frac{\kappa_j \gamma_j^* e^{i\phi_j^{(R)}}}{\eta_j^* \tau_j^* - e^{i\theta_j}}, \quad T_{22}^{(j)} = \frac{\tau_j^* - \eta_j e^{i\theta_j}}{\eta_j^* \tau_j^* - e^{i\theta_j}}. \tag{A4}$$

The phase shifts that appear in Eq. (A4) are related via $\phi_j^{(R)} + \phi_j^{(L)} = \theta_j$, where $\theta_j$ is the round-trip phase shift for the $j$th MRR in the chain.

We rewrite Eqs. (A3) and (A4) in the form

$$\begin{pmatrix} \hat{b}_{j,j+1}^\dagger \\ \hat{d}_{j,j-1}^\dagger \end{pmatrix} = \mathbf{T}^{(j)} \begin{pmatrix} \hat{b}_{j-1,j}^\dagger \\ \hat{d}_{j+1,j}^\dagger \end{pmatrix}. \tag{A5}$$

In this work we treat the case in which all of the MRRs are identical ($\theta_j \to \theta$) and balanced ($\phi_j^{(R)} = \phi_j^{(L)} \to \frac{\theta_j}{2}$). We further assume that the MRRs are all symmetrically and identically coupled,

$$(\tau_j = \eta_j, \kappa_j = \gamma_j) \to (\tau, \kappa). \tag{A6}$$

Finally, without further loss of generality we take the direct transmission coefficients for each of the directional couplers to be real, resulting in Eq. (1) in the main text. With these
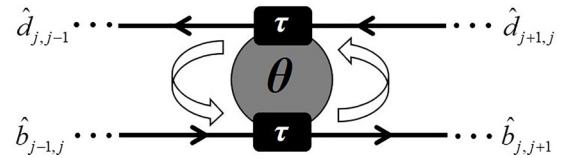
modifications the photonic transfer matrix for the $j$th MRR assumes the form

$$\mathbf{T}^{(j)} \to \frac{\tau^2 e^{i\frac{\theta}{2}} - e^{-i\frac{\theta}{2}}}{1 + \tau^4 - 2\tau^2 \cos\frac{\theta}{2}} \begin{pmatrix} -2i\tau \sin\frac{\theta}{2} & 1 - \tau^2 \\ 1 - \tau^2 & -2i\tau \sin\frac{\theta}{2} \end{pmatrix}. \tag{A7}$$

Figure 5 represents the unit cell of the system we consider after these parametric choices have been imposed.



FIG. 5. The $j$th DB-MRR in a serial chain with arbitrary length $N$. As described in the main text, we have assumed that all of the symmetric, balanced MRRs are identical and that they are identically coupled to the waveguides. We represent each coupling using the real transmission coefficient $\tau$ for the directional couplers involved.

## APPENDIX B: DERIVATION OF THE HOM CONDITION

In order to analyze the photonic transport properties of nontrivial chains ($N > 1$), we must apply the combination rule for $\mathbf{T}$ matrices that properly relates the creation operators describing the input modes to those describing the output modes in accordance with our Heisenberg picture description of the interaction. Referring to the overall transformation matrix for the creation operators due to an MRR chain of length $N$ as $\mathbf{M}_N$,

$$\begin{pmatrix} \hat{a}^\dagger \\ \hat{f}^\dagger \end{pmatrix} = \mathbf{M}_N \begin{pmatrix} \hat{c}^\dagger \\ \hat{l}^\dagger \end{pmatrix}. \tag{B1}$$

Applying the mode-swap algebra that we introduced in [68] suitably tailored to the present $2 \times 2$ case, we express the formal solution for $\mathbf{M}_N$ using

$$\mathbf{M}_N = \mathcal{S}_2^{(2)} \left[ \prod_{j=1}^N \mathcal{S}_2^{(2)} [\mathbf{T}^{(j)}] \right]. \tag{B2}$$

In writing Eq. (B2) we have introduced notation in which $\mathcal{S}_m^{(k)}$ operates on the square matrix $\mathbf{A}$ with dimension $k$ in such a way to produce another square matrix with dimension $k$ appropriate to the linear system with the dependent variable in row $m$ "swapped" with the independent variable from that same row, for example,

$$\text{If} \quad \begin{pmatrix} x' \\ y' \end{pmatrix} = \begin{pmatrix} a & b \\ c & d \end{pmatrix} \begin{pmatrix} x \\ y \end{pmatrix},$$

$$\text{then} \begin{pmatrix} x' \\ y \end{pmatrix} = \mathcal{S}_2^{(2)} \left[ \begin{pmatrix} a & b \\ c & d \end{pmatrix} \right] \begin{pmatrix} x \\ y' \end{pmatrix}. \tag{B3}$$

Working in the lossless, continuous-wave approximation, we analytically derive the one-dimensional HOMM in the serial chain of identical MRRs. The input state to the chain is taken to be

$$|\text{in}\rangle = |1\rangle_a \otimes |1\rangle_f \equiv |1_a, 1_f\rangle = \hat{a}^\dagger \hat{f}^\dagger |\text{vac}\rangle. \tag{B4}$$

According to Eq. (B1), the corresponding output state has the form

$$
\begin{aligned}
|\text{out}\rangle &= [(\mathbf{M}_N)_{11}\hat{c}^\dagger + (\mathbf{M}_N)_{12}\hat{l}^\dagger][(\mathbf{M}_N)_{21}\hat{c}^\dagger + (\mathbf{M}_N)_{22}\hat{l}^\dagger]\,|\text{vac}\rangle \\
&= (\mathbf{M}_N)_{11}(\mathbf{M}_N)_{21}\,|2_c,0_l\rangle + (\mathbf{M}_N)_{12}(\mathbf{M}_N)_{22}\,|0_c,2_l\rangle \\
&\quad + [(\mathbf{M}_N)_{11}(\mathbf{M}_N)_{22} + (\mathbf{M}_N)_{12}(\mathbf{M}_N)_{21}]\,|1_c,1_l\rangle\,, \quad \text{(B5)}
\end{aligned}
$$

making it obvious that the HOM effect is obtained whenever the coefficient of the state $|1_c,1_f\rangle$ vanishes (the permanent of $\mathbf{M}_N$). It is easy to show that the resulting output state is the well-known, properly normalized two-photon NOON state [8],

$$
|2::0;\Phi\rangle = \frac{1}{\sqrt{2}}(|2_c,0_l\rangle + e^{i\Phi}\,|0_c,2_l\rangle). \quad \text{(B6)}
$$

To isolate the HOMM, we consider the output coincidence probability for photons in the state given in Eq. (B5),

$$
P_{1,1}(\tau,\theta;N) = |(\mathbf{M}_N)_{11}(\mathbf{M}_N)_{22} + (\mathbf{M}_N)_{12}(\mathbf{M}_N)_{21}|^2. \quad \text{(B7)}
$$

Using mathematical induction and after some algebraic manipulations, we can show analytically that the probability for output photon coincidence is given by

$$
P_{1,1}(\tau,\theta;N) = \frac{(1 - 4\tau^{2N} + \tau^{4N} + 2\tau^{2N}\cos\theta)^2}{(1 + \tau^{4N} - 2\tau^{2N}\cos\theta)^2}. \quad \text{(B8)}
$$

The HOM constraint can be expressed using

$$
P_{1,1}(\tau,\theta;N) = 0. \quad \text{(B9)}
$$

For a chain of length $N$, Eq. (B9) defines a one-dimensional HOMM $\tau_N(\theta)$. After some more algebra, we find that the physical one-dimensional HOMM for the serial chain of length $N$ is given in closed form by

$$
\tau_N(\theta) = (2 - \cos\theta - \sqrt{3 - 4\cos\theta + \cos^2\theta})^{\frac{1}{2N}}. \quad \text{(B10)}
$$

## APPENDIX C: THE RELATIONSHIP BETWEEN THE TRANSFER MATRICES OF A CONVENTIONAL BEAM SPLITTER AND A MRR

In this Appendix we show how the HOM effect in the MRR can be considered as a generalization of the HOM using a conventional beam splitter.

We model the conventional beam splitter (BS) unitary transfer matrix (between input and output modes) with transmissivity $\cos^2(\theta/2)$ by the $O(2)$ rotation matrix:

$$
\begin{aligned}
&T_{\text{BS}}(\theta) \\
&= \begin{pmatrix} \cos(\theta/2) & \sin(\theta/2) \\ -\sin(\theta/2) & \cos(\theta/2) \end{pmatrix}, \begin{pmatrix} \cos(\theta/2) & i\sin(\theta/2) \\ i\sin(\theta/2) & \cos(\theta/2) \end{pmatrix}, \\
&\hspace{11cm} \text{(C1)}
\end{aligned}
$$

where the phases of the off-diagonal terms are chosen either as $\pm 1$ [Eq. (C1), left] or as $i$ [Eq. (C1), right]. Here, $0 \leqslant \theta \leqslant \pi$ with a balanced 50:50 BS occurring at $\theta = \pi/2$. Note that the HOM effect occurs when the permanent of the matrix $T_{\text{BS}}$ is zero, i.e., $\cos^2(\theta/2) - \sin^2(\theta/2) = \cos(\theta) = 0 \Rightarrow \theta = \pi/2$, the 50:50 BS condition.

Now, a general two-port device (two inputs, two outputs) can be modeled by an $SU(2)$ matrix, which we can always

write in the form

$$
\begin{aligned}
T_{\text{MRR}} &= \begin{pmatrix} T_{11} & T_{12} \\ T_{21} & T_{22} \end{pmatrix} \\
&\rightarrow \begin{pmatrix} |T_{11}|\,e^{i\theta_{11}} & \sqrt{1 - |T_{11}|^2}\,e^{i\theta_{12}} \\ -\sqrt{1 - |T_{11}|^2}\,e^{i\theta_{21}} & |T_{11}|\,e^{i\theta_{22}} \end{pmatrix}, \quad \text{(C2)}
\end{aligned}
$$

which automatically ensures the unitarity requirement that the inner product of each column (row) with itself is 1. Unitarity also requires that the inner product of a column (row) with a different column (row) yields zero. Applying this to Eq. (C2) yields the additional phase constraint

$$
\theta_{11} + \theta_{22} = \theta_{12} + \theta_{21}. \quad \text{(C3)}
$$

An analysis of the HOM effect for an arbitrary dual Fock input state $|n,m\rangle_{ab}$ (with $n$ and $m$ both odd) reveals that any arbitrary choice of phases satisfying the above phase constraint (C3) also yields the HOM effect (and, in fact, a more generalized version of it) for the complete destructive interference of the quantum amplitude for output coincidence counts [69].

Using Eq. (C2), the ordinary BS (C1) is recovered by choosing $T_{11} = \cos(\theta/2)$ (transmission amplitude) with $0 \leqslant \theta \leqslant \pi$ and the phase choices of either $\theta_{ij} = 0$ for the left part of Eq. (C1) or $\{\theta_{11} = \theta_{22} = 0, \theta_{12} = \pi/2, \theta_{21} = -\pi/2\}$ for the right part of Eq. (C1).

For the MRR, we have from Eq. (A4)

$$
\left|T_{11}^{(j)}\right| = \left|\frac{\eta_j^* - \tau_j e^{i\theta_j}}{\eta_j^* \tau_j^* - e^{i\theta_j}}\right| \equiv \cos(\varphi/2), \quad \text{(C4)}
$$

where $\cos(\varphi) = \cos[\varphi(\eta_j,\tau_j,\theta_j)]$ is a Fabry-Pérot-like function of the upper ($\eta_j$) and lower ($\tau_j$) physical beam splitter transmission coefficients of the ($j$th) MRR and $\theta_j$ is the round-trip phase angle. But as discussed above, the particular values of the phases $\theta_{ij}$ of $T_{ij} = |T_{ij}|\,e^{i\theta_{ij}}$ do not affect the HOM effect, as long as they satisfy the phase constraint (C3). (Note that in $T_{21}$ we have already factored out a crucial $-1$ in its definition). Thus, if we, for a moment, chose the phases to be $\theta_{ij} = 0$, then $T_{\text{MRR}}$ would have the form of an *effective* conventional BS:

$$
T_{\text{MRR}} \xrightarrow{\theta_{ij} \to 0} \begin{pmatrix} \cos(\varphi/2) & \sin(\varphi/2) \\ -\sin(\varphi/2) & \cos(\varphi/2) \end{pmatrix}. \quad \text{(C5)}
$$

It is in the sense of Eq. (C5) with the definition (C4) that we mean that the MRR "acts like" an expansion of the conventional BS [with transmission coefficient $\cos(\theta/2)$] to two BSs (with transmission coefficients $\eta_j$ and $\tau_j$), plus an internal phase angle $\theta_j$.

Finally, for the MRR, the HOM effect also occurs when the permanent of the matrix $T_{\text{MRR}}$ is zero, i.e., $|T_{11}|^2 e^{i(\theta_{11}+\theta_{22})} - (1 - |T_{11}|^2)e^{i(\theta_{12}+\theta_{21})} = 0 \Rightarrow 2|T_{11}|^2 - 1 = 2\cos(\varphi/2)^2 - 1 = \cos(\varphi) = 0$, where we have used $|T_{11}| \equiv \cos(\varphi/2)$ and the phase constraint (to factor out the phases). Thus, for the MRR the HOM effect occurs for the effective BS angle condition $\varphi = \pi/2$, which by Eq. (C4) is a complicated function of the MRR upper and lower physical beam splitters and round-trip phase angle. The fact that the MRR HOM condition $\varphi(\eta_j,\tau_j,\theta_j) = \pi/2$ occurs in a larger parameter space is what gives rise to a manifold of HOM solutions (hence the term HOMM) vs the single-point solution $\theta = \pi/2$ for the conventional BS.

[1] C. K. Hong, Z. Y. Ou, and L. Mandel, Measurement of Subpicosecond Time Intervals between Two Photons by Interference, Phys. Rev. Lett. **59**, 2044 (1987).

[2] H. Fearn and R. Loudon, Quantum theory of the lossless beam splitter, Opt. Commun. **64**, 485 (1987).

[3] J. G. Rarity and P. R. Tapster, Fourth-order interference in parametric downconversion, J. Opt. Soc. Am. B **6**, 1221 (1989).

[4] I. Abram, R. K. Raj, J. L. Oudar, and G. Dolique, Direct Observation of the Second-Order Coherence of Parametrically Generated Light, Phys. Rev. Lett. **57**, 2516 (1986).

[5] Y. H. Shih and C. O. Alley, New Type of Einstein-Podolsky-Rosen-Bohm Experiment Using Pairs of Light Quanta Produced by Optical Parametric Down Conversion, Phys. Rev. Lett. **61**, 2921 (1988).

[6] A. Einstein, B. Podolsky, and N. Rosen, Can quantum-mechanical description of physical reality be considered complete? Phys. Rev. **47**, 777 (1935).

[7] A. K. Ekert, Quantum Cryptography Based on Bell's Theorem, Phys. Rev. Lett. **67**, 661 (1991).

[8] J. P. Dowling, Quantum optical metrology - the lowdown on high-n00n states, Contemp. Phys. **49**, 125 (2008).

[9] V. Giovannetti, S. Lloyd, and L. Maccone, Advances in quantum metrology, Nat. Photonics **5**, 222 (2011).

[10] P. Kok, W. J. Munro, K. Nemoto, T. C. Ralph, J. P. Dowling, and G. J. Milburn, Linear optical quantum computing with photonic qubits, Rev. Mod. Phys. **79**, 135 (2007).

[11] F. Bouchard, A. Sit, Y. Zhang, R. Fickler, F. M. Miatto, Y. Yao, F. Sciarrino, and E. Karimi, Two-photon interference: The Hong–Ou–Mandel effect, Rep. Prog. Phys. **84**, 012402 (2021).

[12] E. Knill, R. Laflamme, and G. J. Milburn, A scheme for efficient quantum computation with linear optics, Nature (London) **409**, 46 (2001).

[13] R. E. Scott, P. M. Alsing, A. M. Smith, M. L. Fanto, C. C. Tison, J. Schneeloch, and E. E. Hach, III, Scalable controlled-NOT gate for linear optical quantum computing using microring resonators, Phys. Rev. A **100**, 022322 (2019).

[14] R. Okamoto, J. L. O'Brien, H. F. Hofmann, and S. Takeuchi, Realization of a Knill-Laflamme-Milburn controlled-not photonic quantum circuit combining effective optical nonlinearities, Proc. Natl. Acad. Sci. USA **108**, 10067 (2011).

[15] K. A. G. Fisher, A. Broadbent, L. K. Shalm, Z. Yan, J. Lavoie, R. Prevedel, T. Jennewein, and K. J. Resch, Quantum computing on encrypted data, Nat. Commun. **5**, 3074 (2014).

[16] A. W. Harrow, A. Hassidim, and S. Lloyd, Quantum Algorithm for Linear Systems of Equations, Phys. Rev. Lett. **103**, 150502 (2009).

[17] X.-D. Cai, C. Weedbrook, Z.-E. Su, M.-C. Chen, M. Gu, M.-J. Zhu, L. Li, N.-L. Liu, C.-Y. Lu, and J.-W. Pan, Experimental Quantum Computing to Solve Systems of Linear Equations, Phys. Rev. Lett. **110**, 230501 (2013).

[18] S. Weimann, A. Perez-Leija, M. Lebugle, R. Keil, M. Tichy, M. Gräfe, R. Heilmann, S. Nolte, H. Moya-Cessa, G. Weihs, D. N. Christodoulides, and A. Szameit, Implementation of quantum and classical discrete fractional fourier transforms, Nat. Commun. **7**, 11027 (2016).

[19] P. C. Humphreys, B. J. Metcalf, J. B. Spring, M. Moore, X.-M. Jin, M. Barbieri, W. S. Kolthammer, and I. A. Walmsley, Linear Optical Quantum Computing in a Single Spatial Mode, Phys. Rev. Lett. **111**, 150501 (2013).

[20] R. Kaltenbaek, B. Blauensteiner, M. Żukowski, M. Aspelmeyer, and A. Zeilinger, Experimental Interference of Independent Photons, Phys. Rev. Lett. **96**, 240502 (2006).

[21] P. J. Mosley, J. S. Lundeen, B. J. Smith, P. Wasylczyk, A. B. U'Ren, C. Silberhorn, and I. A. Walmsley, Heralded Generation of Ultrafast Single Photons in Pure Quantum States, Phys. Rev. Lett. **100**, 133601 (2008).

[22] K. Sanaka, A. Pawlis, T. D. Ladd, K. Lischka, and Y. Yamamoto, Indistinguishable Photons from Independent Semiconductor Nanostructures, Phys. Rev. Lett. **103**, 053601 (2009).

[23] E. B. Flagg, A. Muller, S. V. Polyakov, A. Ling, A. Migdall, and G. S. Solomon, Interference of Single Photons from Two Separate Semiconductor Quantum Dots, Phys. Rev. Lett. **104**, 137401 (2010).

[24] R. B. Patel, A. J. Bennett, I. Farrer, C. A. Nicoll, D. A. Ritchie, and A. J. Shields, Two-photon interference of the emission from electrically tunable remote quantum dots, Nat. Photonics **4**, 632 (2010).

[25] Y.-J. Wei, Y.-M. He, M.-C. Chen, Y.-N. Hu, Y. He, D. Wu, C. Schneider, M. Kamp, S. Höfling, C.-Y. Lu, and J.-W. Pan, Deterministic and robust generation of single photons from a single quantum dot with 99.5% indistinguishability using adiabatic rapid passage, Nano Lett. **14**, 6515 (2014).

[26] P. Senellart, G. Soloman, and A. White, High-performance semiconductor quantum-dot single-photon sources, Nat. Nanotechnol. **12**, 1026 (2017).

[27] D. Felinto, C. W. Chou, J. Laurat, E. W. Schomburg, H. de Riedmatten, and H. J. Kimble, Conditional control of the quantum states of remote atomic memories for quantum networking, Nat. Phys. **2**, 844 (2006).

[28] T. Chanelière, D. N. Matsukevich, S. D. Jenkins, S.-Y. Lan, R. Zhao, T. A. B. Kennedy, and A. Kuzmich, Quantum Interference of Electromagnetic Fields from Remote Quantum Memories, Phys. Rev. Lett. **98**, 113602 (2007).

[29] Z.-S. Yuan, Y.-A. Chen, S. Chen, B. Zhao, M. Koch, T. Strassel, Y. Zhao, G.-J. Zhu, J. Schmiedmayer, and J.-W. Pan, Synchronized Independent Narrow-Band Single Photons and Efficient Generation of Photonic Entanglement, Phys. Rev. Lett. **98**, 180503 (2007).

[30] Z.-S. Yuan, Y.-A. Chen, B. Zhao, S. Chen, J. Schmiedmayer, and J.-W. Pan, Experimental demonstration of a BDCZ quantum repeater node, Nature (London) **454**, 1098 (2008).

[31] Y.-A. Chen, S. Chen, Z.-S. Yuan, B. Zhao, C.-S. Chuu, J. Schmiedmayer, and J.-W. Pan, Memory-built-in quantum teleportation with photonic and atomic qubits, Nat. Phys. **4**, 103 (2008).

[32] H. Bernien, L. Childress, L. Robledo, M. Markham, D. Twitchen, and R. Hanson, Two-Photon Quantum Interference from Separate Nitrogen Vacancy Centers in Diamond, Phys. Rev. Lett. **108**, 043604 (2012).

[33] A. Sipahigil, M. L. Goldman, E. Togan, Y. Chu, M. Markham, D. J. Twitchen, A. S. Zibrov, A. Kubanek, and M. D. Lukin, Quantum Interference of Single Photons from Remote Nitrogen-Vacancy Centers in Diamond, Phys. Rev. Lett. **108**, 143601 (2012).

[34] A. Sipahigil, K. D. Jahnke, L. J. Rogers, T. Teraji, J. Isoya, A. S. Zibrov, F. Jelezko, and M. D. Lukin, Indistinguishable Photons from Separated Silicon-Vacancy Centers in Diamond, Phys. Rev. Lett. **113**, 113602 (2014).

[35] A. Kiraz, M. Ehrl, T. Hellerer, O. E. Müstecaplıoğlu, C. Bräuchle, and A. Zumbusch, Indistinguishable Photons from a Single Molecule, Phys. Rev. Lett. **94**, 223602 (2005).

[36] R. Lettow, Y. L. A. Rezus, A. Renn, G. Zumofen, E. Ikonen, S. Götzinger, and V. Sandoghdar, Quantum Interference of Tunably Indistinguishable Photons from Remote Organic Molecules, Phys. Rev. Lett. **104**, 123605 (2010).

[37] J. Beugnon, M. P. A. Jones, J. Dingjan, B. Darquié, G. Messin, A. Browaeys, and P. Grangier, Quantum interference between two single photons emitted by independently trapped atoms, Nature (London) **440**, 779 (2006).

[38] H. P. Specht, C. Nölleke, A. Reiserer, M. Uphoff, E. Figueroa, S. Ritter, and G. Rempe, A single-atom quantum memory, Nature (London) **473**, 190 (2011).

[39] P. Maunz, D. L. Moehring, S. Olmschenk, K. C. Younge, D. N. Matsukevich, and C. Monroe, Quantum interference of photon pairs from two remote trapped atomic ions, Nat. Phys. **3**, 538 (2007).

[40] N. Gisin, G. Ribordy, W. Tittel, and H. Zbinden, Quantum cryptography, Rev. Mod. Phys. **74**, 145 (2002).

[41] S. Pirandola, U. L. Andersen, L. Banchi, M. Berta, D. Bunandar, R. Colbeck, D. Englund, T. Gehring, C. Lupo, C. Ottaviani, J. L. Pereira, M. Razavi, J. S. Shaari, M. Tomamichel, V. C. Usenko, G. Vallone, P. Villoresi, and P. Wallden, Advances in quantum cryptography, Adv. Opt. Photonics **12**, 1012 (2020).

[42] L. Lydersen, C. Wiechers, C. Wittmann, D. Elser, J. Skaar, and V. Makarov, Hacking commercial quantum cryptography systems by tailored bright illumination, Nat. Photonics **4**, 686 (2010).

[43] I. Gerhardt, Q. Liu, A. Lamas-Linares, J. Skaar, C. Kurtsiefer, and V. Makarov, Full-field implementation of a perfect eavesdropper on a quantum cryptography system, Nat. Commun. **2**, 349 (2011).

[44] D. Mayers and A. Yao, Quantum cryptography with imperfect apparatus, in *Proceedings of the 39th Annual Symposium on Foundations of Computer Science, FOCS '98* (IEEE Computer Society, Washington, DC, 1998), p. 503.

[45] A. Acín, N. Brunner, N. Gisin, S. Massar, S. Pironio, and V. Scarani, Device-Independent Security of Quantum Cryptography against Collective Attacks, Phys. Rev. Lett. **98**, 230501 (2007).

[46] S. L. Braunstein and S. Pirandola, Side-Channel-Free Quantum Key Distribution, Phys. Rev. Lett. **108**, 130502 (2012).

[47] H.-K. Lo, M. Curty, and B. Qi, Measurement-Device-Independent Quantum Key Distribution, Phys. Rev. Lett. **108**, 130503 (2012).

[48] Y. Liu, T.-Y. Chen, L.-J. Wang, H. Liang, G.-L. Shentu, J. Wang, K. Cui, H.-L. Yin, N.-L. Liu, L. Li, X. Ma, J. S. Pelc, M. M. Fejer, C.-Z. Peng, Q. Zhang, and J.-W. Pan, Experimental Measurement-Device-Independent Quantum Key Distribution, Phys. Rev. Lett. **111**, 130502 (2013).

[49] J.-Y. Guan, Z. Cao, Y. Liu, G.-L. Shen-Tu, J. S. Pelc, M. M. Fejer, C.-Z. Peng, X. Ma, Q. Zhang, and J.-W. Pan, Experimental Passive Round-Robin Differential Phase-Shift Quantum Key Distribution, Phys. Rev. Lett. **114**, 180502 (2015).

[50] J. Hofmann, M. Krug, N. Ortegel, L. Gérard, M. Weber, W. Rosenfeld, and H. Weinfurter, Heralded entanglement between widely separated atoms, Science **337**, 72 (2012).

[51] A. Narla, S. Shankar, M. Hatridge, Z. Leghtas, K. M. Sliwa, E. Zalys-Geller, S. O. Mundhada, W. Pfaff, L. Frunzio, R. J. Schoelkopf, and M. H. Devoret, Robust Concurrent Remote Entanglement Between Two Superconducting Qubits, Phys. Rev. X **6**, 031036 (2016).

[52] N. Sangouard, C. Simon, H. de Riedmatten, and N. Gisin, Quantum repeaters based on atomic ensembles and linear optics, Rev. Mod. Phys. **83**, 33 (2011).

[53] C.-H. F. Fung, B. Qi, K. Tamaki, and H.-K. Lo, Phase-remapping attack in practical quantum-key-distribution systems, Phys. Rev. A **75**, 032314 (2007).

[54] Y. Zhao, C.-H. F. Fung, B. Qi, C. Chen, and H.-K. Lo, Quantum hacking: Experimental demonstration of time-shift attack against practical quantum-key-distribution systems, Phys. Rev. A **78**, 042333 (2008).

[55] D. A. B. Miller, Perfect optics with imperfect components, Optica **2**, 747 (2015).

[56] S. B. R. Hammerly and D. Englund, Asymptotically fault-tolerant programs photonics, Nat. Commun. **13**, 6831 (2022).

[57] R. Hamerly, S. Bandyopadhyay, and D. Englund, Accurate Self-Configuration of Rectangular Multiport Interferometers, Phys. Rev. Appl. **18**, 024019 (2022).

[58] J. Mower, N. C. Harris, G. R. Steinbrecher, Y. Lahini, and D. Englund, High-fidelity quantum state evolution in imperfect photonic integrated circuits, Phys. Rev. A **92**, 032322 (2015).

[59] J. C. Mikkelsen, W. D. Sacher, and J. K. S. Poon, Dimensional variation tolerant silicon-on-insulator directional couplers, Opt. Express **22**, 3145 (2014).

[60] E. E. Hach, III, S. F. Preble, A. W. Elshaari, P. M. Alsing, and M. L. Fanto, Scalable Hong-Ou-Mandel manifolds in quantum-optical ring resonators, Phys. Rev. A **89**, 043805 (2014).

[61] P. M. Alsing, E. E. Hach, III, C. C. Tison, and A. M. Smith, A quantum optical description of losses in ring resonators based on field operator transformations, Phys. Rev. A **95**, 053828 (2017).

[62] A. Yariv, Universal relations for coupling of optical power between microresonators and dielectric waveguides, Electron. Lett. **36**, 321 (2000).

[63] P. M. Alsing and E. E. Hach, III, Photon-pair generation in a lossy microring resonator. I. Theory, Phys. Rev. A **96**, 033847 (2017).

[64] P. M. Alsing and E. E. Hach, III, Photon-pair generation in a lossy microring resonator. II. Entanglement in the output mixed Gaussian squeezed state, Phys. Rev. A **96**, 033848 (2017).

[65] J. Skaar, J. Escartin, and H. Landro, Quantum mechanical description of linear optics, Am. J. Phys. **72**, 1385 (2004).

[66] R. Millman and G. Parker, *Elements of Differential Geometry* (Prentice Hall, New York, 1977).

[67] M. G. Raymer and C. J. McKinstrie, Quantum input-output theory for optical cavities with arbitrary coupling strength: Application to two-photon wave-packet shaping, Phys. Rev. A **88**, 043819 (2013).

[68] P. L. Kaulfuss, P. M. Alsing, E. E. Hach, III, A. M. Smith, and M. L. Fanto, Direct interferometric test of the nonlinear phase-shift gate, Phys. Rev. A **103**, 022405 (2021).

[69] P. M. Alsing, R. J. Birrittella, C. C. Gerry, J. Mimih, and P. L. Knight, Extending the Hong-Ou-Mandel effect: The power of nonclassicality, Phys. Rev. A **105**, 013712 (2022).